Specific Targeting MRI of Chitosan Oligosaccharide Modified Fe$_3$O$_4$ Nanoprobe on Macrophage and the Inhibition of Macrophage Foaming Induced by ox-LDL

Xu Cao[1,2]   Ke Ma[1]   Yuhao Tao[1]   Deyang Xi[1]   Fangyu Hu[1]   Jingjing Li[1,2*]

1. School of Medical Imaging, Xuzhou Medical University, Xuzhou, Jiangsu, 221006, China
2. Department of Radiology, the Affiliated Hospital of Xuzhou Medical University, Xuzhou, Jiangsu, 221002, China

ABSTRACT

Atherosclerosis (AS) is a primary cause of morbidity and mortality all over the world. Molecular imaging techniques can enable early localization and diagnosis of atherosclerosis plaques. Recent newly developed chitooligosaccharides (CSO) is considered to be capable of target mannose receptors on the surface of macrophages and to inhibit foam cell formation. Here we present a targeting magnetic resonance imaging (MRI) nanoprobe, which was successfully constructed with polyacrylic acid (PAA) modified nanometer iron oxide (Fe$_3$O$_4$) as the core, and coating with CSO molecules, possessing the abilities of targeted MRI and specifically inhibition of the formation of foamy macrophages in the atherosclerotic process. The experimental results showed that the distributions of PAA-Fe$_3$O$_4$ and CSO-PAA-Fe$_3$O$_4$ were uniform and the corresponding sizes were about 5.93 nm and 8.15 nm, respectively. The Fourier transform infrared spectra (FTIR) testified the CSO was coupled with PAA-Fe$_3$O$_4$ successfully. After coupled with CSO, the r_1 of PAA-Fe$_3$O$_4$ was increased from 5.317 mM s^{-1} to 6.147 mM s^{-1}, indicating their potential as MRI contrast agent. Oil Red O staining and total cholesterols (TC) determination showed that CSO-PAA-Fe$_3$O$_4$ could significantly inhibit the foaming process of RAW264.7 cells induced by oxidatively modified low density lipoprotein (ox-LDL). *In vitro* cellular MRI displayed that, compared with PAA-Fe$_3$O$_4$, CSO-PAA-Fe$_3$O$_4$ could lower the T$_1$ relaxation time of RAW264.7 cells better. In summary, construction of CSO-PAA-Fe$_3$O$_4$ nanoprobe in this study could realize the targeted MRI of macrophages and inhibition of ox-LDL induced macrophage foaming process. This will provide a new avenue in the diagnosis and treatment of AS.

1. Introduction

AS is a disease accompanied by an autoimmune response to low-density lipoprotein (LDL) that causes strokes, ischemic heart diseases, and peripheral vascular diseases etc., which has been one of the most usual chronic fatal causes in aged people. Early diagnosis, prevention, and further accumulation inhibition of atherosclerotic plaque have become the main directions of cardiovascular disease research.

In the medical imaging evaluation of atherosclerotic lesions, medical imaging apparatus such as ultrasound,

Corresponding Author:
Jingjing Li,
School of Medical Imaging, Xuzhou Medical University, Xuzhou, Jiangsu, 221006, China; Department of Radiology, the Affiliated Hospital of Xuzhou Medical University, Xuzhou, Jiangsu, 221002, China;
Email: qingchao0124@163.com

MRI, computerized tomography (CT), and nuclear medicine have made remarkable breakthroughs over time [1-4]. Among them, MRI as a non-invasive diagnosis mode has been well applied to analyze the degree of stenosis, vessel wall thickness, and plaque size. It should be mentioned that although MRI has sufficient spatial resolution and good signal-to-noise ratio, however, it is not specific enough to characterize the composition of atherosclerotic plaques [5]. Therefore, application of MR for the assessment of AS, especially at an early stage, has significant limitations. In recent years, the rapid development of molecular MRI nanoprobe has become an essential tool for studying AS under its advantages [6], including non-invasive, radiation-free, multiplanar imaging, multi-serial imaging, and high soft-tissue resolution, providing a new approach for the early detection of AS plaques [7].

Iron oxide as MRI contrast agent coupling with the targeting molecules has been used in vascular imaging, macrophage uptake, cell labeling, and cancer hyperthermia [8-12]. Since common iron oxide nanoparticles are easily phagocytosed by peripheral phagocytes during circulation due to physical properties as well as biological characteristics, which may weaken their imaging performance. In order to enhance the biological compatibility and evade particle agglomerations, polymers, little molecules, surfactants, and others are commonly used to clad nanoparticles. Iron oxide magnetic nanoparticles have been employed as T_2 contrast medium, giving a negative comparison diagram in the ordinary way. In clinically, T_2-weighted images (T_2WI) were used to examine organ pathological changes, but these were more prone to motion artifact from longer acquisition times. T_2WI needs a longer repetition time (TR) and echo time (TE) than T_1-weighted images (T_1WI) as well as clearer T_2 images require more advanced MRI equipment, which all greatly increase the cost of clinical examination. Based on the presence of a high-intensity signal within the embolus or intraplaque hemorrhage caused by methemoglobin T_1 shortening, the plaque characterization with T_1WI in MR has facile plaque imaging [13]. With the function of their sizes, superparamagnetic iron oxide nanoparticles (SPIO NPs) may provide a positive contrast in T_1WI [14]. At the same time, it is different from gadolinium-containing contrast agents, which are cytotoxic and tend to accumulate in tissues organs. Iron oxide nanoparticles provide a safer gadolinium-free T_1 contrast agent for MR imaging [15]. In this work, we synthesized PAA modified SPIO NPs as T_1 MRI contrast agent.

Macrophages have been the most extensively studied target to study AS plaques. Numerous studies have shown that macrophages were involved in the process of AS development and were closely related to plaque stability, playing an essential regulatory role in the atherosclerotic

pathological process [16]. In the early stage of the disease, inflammatory cells such as monocytes and macrophages enter the damaged blood vessel wall under the chemotactic action of various inflammatory factors and phagocytize lipids to become foam cells. In the late stage of the disease, macrophages, foam cells, lymphocytes, and mast cells are the main components of AS plaques, with macrophages and lymphocytes being the main cellular components in ruptured plaques. CSO are oligomers of chitosan and consist of 3 to 10 units of N-acetylglucosamine or glucosamine. The CSO has been reported to interact with mannose receptors on the surface of macrophages through N-acetylglucosamine structures [17]. The mannose receptors on macrophages are consisted of extracellular cysteine-rich region (CR), type II fibronectin region (FN II), and C-type lectin-like region (CTLD). Especially, in the CTLD chains of extracellular mannose receptor, CTLD4 can recognize and bind the N-acetylglucosamine residues of CSO in CTLD1 - 8. At the same time, with the synergistic participation of CTLD5-8, mannose receptors can bind to ligands more closely and firmly [18]. Miraculously, CSO binding to macrophages significantly enhanced the abundant adenosine triphosphate-binding cassette transporter A1 (ABCA1) on the surface of macrophages, mediating cholesterol efflux out of the cell, and reversing the transport of cholesterol mediated by ABCA1 bound to Apolipoprotein A1 (ApoA1) and high-density lipoprotein (HDL), resulting in a significant decrease in intracellular cholesterol levels. It has also been found that CSO promotes intracellular cholesterol efflux while increasing the level of macrophage autophagy and further inhibiting macrophage frothing [19,20]. Besides retaining the excellent biocompatibility and non-biotoxicity of chitosan, CSO keeps better water solubility and extral biological activities, including antibacterial, antifungal, antiviral, anti-tumor, exert fat, blood pressure control and hypocholesteromic effects [21], which have been widely used in antitumor and antioxidant applications [22,23]. Meanwhile, CSO nanoparticles possess lower haemolysin activity, cytotoxicity and the high encapsulation efficiency made them as an effective carrier [24]. Thus, CSO is expected to be used as the targeting molecule and therapy drug for AS.

In this report, we simply conjugated PAA modified Fe_3O_4 nanoparticles (PAA-Fe_3O_4) with CSO to fabricate the theranostic nanoprobe for AS. Such conjugation was realized *via* amide bonds between carboxyl groups on the surface of PAA-Fe_3O_4 and amino groups of CSO (Figure 1a). CSO not only directs PAA-Fe_3O_4 to bind smoothly to the foaming macrophages *via* mannose receptors (Figure 1b) and achieves enhanced MR imaging by endocytosis (Figure 1c), but also effectively inhibits the further development of macrophages

toward foam cells by promoting the out-cell transport of accumulated lipids within the macrophages and reducing the cholesterol content of the cells. The introduction of a CSO coating on the surface of iron oxide nanoparticles will greatly increase biocompatibility, thus facilitating the biomedical application of these nanoparticles and providing new ideas for the diagnosis and treatment of AS.

2. Materials and Methods

Materials

PAA was purchased from Aladdin Co., Ltd (Shanghai, China). Ferric chloride·Hexahydrate ($FeCl_3·6H_2O$) was acquired from Wokai Biotech Co., Ltd (Shandong, China). Ferrous sulfate·Heptahydrate ($FeSO_4·7H_2O$) was purchased from Meilunbio Co., Ltd (Shanghai, China). Both 1-ethyl-3-(3-dimethylaminopropyl)carbodiimide (EDC) and N-hydroxysuccinimide (NHS) were obtained from Sigma-Aldrich (America). CSO (average molecular weight <1000) was ordered from Dibai Biotech Co., Ltd (Shanghai, China). RPMI1640 medium was got from Keygen Biotech Co., Ltd (Jiangsu, China). Ox-LDL was collected from Yuanye Biotechnology Co., Ltd (Beijing, China). The whole cholesterol detection kit was acquired from Suoqiao Biotech Co., Ltd (Beijing, China). Mouse mononuclear macrophage leukemia cells (RAW264.7) were obtained from the Cell Bank of the Chinese Academy of Sciences (Shanghai, China).

Synthesis of PAA modified Fe_3O_4 nanoparticles

The synthetic approach for PAA-Fe_3O_4 was referred to a literature previously reported by Kucheryavy *et al*. [25]. Briefly, a 20 mL amount of 4 mg/mL PAA solution was
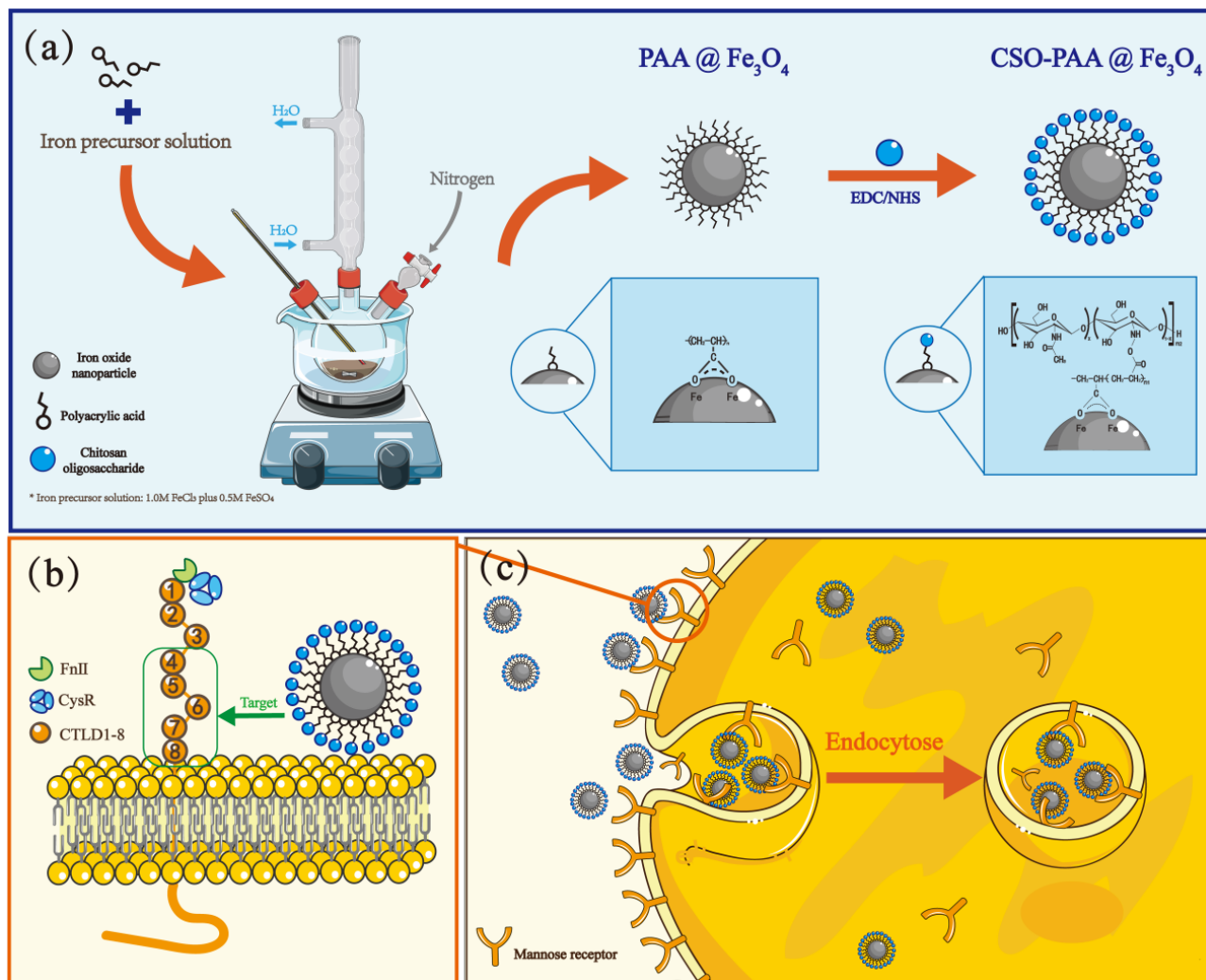
Figure 1. Schematic illustration of the synthesis route of CSO-PAA-Fe_3O_4 nanoprobe (a). The mannose receptor on macrophage surface is composed of CR, FN II and CTLDs. Among them, CTLD4-8 can specifically recognize and bind the N-acetylglucosamine residue of CSO, (b). Endocytosis of CSO-PAA-Fe_3O_4 by macrophages (c).

first to remove oxygen by purgeding (≥50 min)with nitrogenand was heated to 100℃ with a magnetic stirrer. After that, 0.4 mL of $FeCl_3$ & $FeSO_4$ solution (1.0 mol/L $FeCl_3$ and 0.5 mol/L $FeSO_4$) was quickly injected, followed by the addition of 9.0 mL of 28% ammonia solution. After stirred for 15 minutes, 0.6 mL of the $FeCl_3$ & $FeSO_4$ solution and 4.0 mL of ammonia solution were infused into the mixed solution every 15 minutes for four times. The obtained solutions were cooled to air temperature and dialyzed (MW=10000) for 72 hours in ultrapure water to remove unreacted raw materials. The PAA-Fe_3O_4 nanoparticles were stored at 4℃ for use.

Conjugation of CSO to PAA-Fe_3O_4 nanoparticles

The carboxyl groups of PAA-Fe_3O_4 were first activated by EDC. In details, 200 mg EDC and 10 mL amount of PAA-Fe_3O_4 solution was magnetically stirred at indoor temperature for 15 min. Then, 1 g CSO, and 100 mg NHS were added to the mixed solution and reacted at 37°C for two hours. The obtained solutions were dialyzed (MW=3000) for 48 hours in ultrapure water. The obtained CSO-PAA-Fe_3O_4 solution was stored at 4℃ before use.

Charaterization of PAA-Fe_3O_4 nanoparticles andCSO-PAA-Fe_3O_4 nanoprobes

The transmission electron microscopy (TEM) images, fourier transform infrared (FTIR) spectra and surface zeta potential as well as the hydrodynamic diameters of fabricated nanoprobe were determined. For TEM characterization, 10 μL amount of PAA-Fe_3O_4 andCSO-PAA-Fe_3O_4solution was dropped onto carbon-coated copper grids, respectively. After dried, copper grids were ready for TEM observation and photography. For FTIR scanning, dried PAA-Fe_3O_4 and CSO-PAA-Fe_3O_4 powders were dispersed in potassium bromide (KBr) powder to prepare tablets. The TENSOR27 Fourier transform infrared spectrometer was used for scanning in the range of 500-2000 cm^{-1}. To analyze the surface zeta potential, 1 mL of PAA-Fe_3O_4 and CSO-PAA-Fe_3O_4 solution was placed into the sample cell and analyzed by the Zetasizer Nano ZS90 nanoparticle potential analyzer, respectively.

Determination of iron concentration

The concentration of iron ions was tested by inductively coupled plasma-mass spectrometry (ICP-MS)(Optima 5300DV, PerkinElmer, USA). 50 μL of PAA-Fe_3O_4 and CSO-PAA-Fe_3O_4 solutions were mixed with 50 μL of concentrated nitric acid and placed in an oven at 80℃ for 30 min, respectively. Then, 350 μL of 5% dilute nitric acid and 1.6 mL of H_2O were added to determine iron ion concentration by ICP.

T_1 relaxivity determinations of PAA-Fe_3O_4 and CSO-PAA-Fe_3O_4

The T_1 relaxation time of PAA-Fe_3O_4 (0.066, 0.133, 0.266, 0.399, 0.532 mmol/L) and CSO-PAA-Fe_3O_4 (0.253, 0.337, 0.422, 0.506, 0.675 mmol/L) at different iron ion concentrations were measured by MR scanning. The scanning parameters were settled as follows. For T_1WI, TR 425 ms, TE 14.0 ms, reversal time 200~800 ms, matrix 384 × 224, field of view (FOV) 18 × 18 cm, layer thickness 3.0 mm, layer distance 1.5 mm. The original T_1-map image was processed by GE Aw4.2 workstation to obtain the T_1 relaxation time. The corresponding linear regression equations were plotted using the iron ion concentration as horizontal coordinates and the reciprocal of the samples' T_1 relaxation time at different concentrations as ordinate to calculate the T_1 relaxation rates.

In vitrocell viability

RAW264.7 cells at logarithmic growth stage were inoculated in two 96-well plates at a concentration of 2×10^4 cells/mL, followed by incubating at 37℃ for 24 hours. PAA-Fe_3O_4 or CSO-PAA-Fe_3O_4 with different concentrations of Fe^{3+} (0, 0.05, 0.1, 0.15, 0.2, 0.25, 0.3, 0.35, 0.4, 0.45, and 0.5 mmol/L) were incubated with RAW264.7 cells for 24 hours, respectively. After discarding the nanomaterials and washing the cells in 96-well plates with PBS for three times, a 100 μL of 5 mg/mL MTT solution was injectedinto each well and placed at 37 ℃ for four hours. Finally, 100 μL of dimethyl sulfoxide (DMSO) was added to dissolve the purple crystals, and the absorbance value of each well was measured at 490 nm by the microplate analyzer.

Effect of of CSO-PAA-Fe_3O_4 on the inhibition of macrophage foaming determined by Oil red O staining

6 mL of oil red O solution was diluted to 10 mL in a tube. After standing for 10 min, it was filtered in the dark. 60 μg/mL ox-LDL pretreated RAW264.7 cells were treated with PAA-Fe_3O_4 or CSO-PAA-Fe_3O_4 (Fe^{3+} concentration: 0, 0.15, 0.25, and 0.35 mmol/L) for 48 hours. After fixed with 4% paraformaldehyde for 15 min and rinsed twice with PBS, 500 μL oil red O working solution was added to each well. Dye in the dark for 40 min, and rinse with distilled water twice. The 24-well plates were the placed under an inverted fluorescence microscope (LEICA) for observation. The obtained images were further analyzed using ImageJ software.

Effect of CSO-PAA-Fe$_3$O$_4$ on the inhibition of macrophage foaming byTC determination

60 µg/mL ox-LDL pretreated RAW264.7 cells were treated with PAA-Fe$_3$O$_4$ or CSO-PAA-Fe$_3$O$_4$ (Fe^{3+} concentration of 0, 0.15, 0.25, and 0.35 mmol/L) for 48 hours. The TC amount in RAW264.7 cells were determined following the Total Cholesterol Assay kit instructions. Briefly, 400~500 million cells were collected and centrifuged at 1000 rpm for 20 min. After discarding the supernatant, 1 mL of isopropanol was added and the cells were ultrasonic crushed for 1 min (intensity 20%, ultrasonic 2 s, stop 1 s). Then, the supernatant after centrifugation was collected as TC liquid to be tested. For TC detection, 50 µL TC standard, 50 µL TC sample solution, and 150 µL TC working solution were added into 96-well plate. After standing for 24 hours, the absorbance value was measured at 500 nm by the microplate analyzer. The OD value of each well was measured and the TC content in the cells was calculated according to the formula:

TC (µmol/10^4 cells) = C (standard solution) × OD (assay tube) / OD (standard tube) / cell volume (10^4 cells)

C (standard liquid) = 0.5 µmol/mL

In vitro specific MRI

RAW264.7 cells were incubated with PAA-Fe$_3$O$_4$ or CSO-PAA-Fe$_3$O$_4$ with different Fe^{3+} concentrations of 0, 0.25, and 0.35 mmol/L at 37 ℃ for two hours. After washed twice with PBS, trypsinized with EDTA-trypsin, and then suspended in 1% sepharose for MRI scanning. GE Signa 3.0 T whole-body magnetic resonance imager and a small animal coil were used for T$_1$WI scanning.

Statistical analysis

Statistical analysis was performed using *SPSS* software (version 24.0), and data conforming to a normal distribution are denoted by $`X \pm S$. Independent samples *t*-test was used for comparison between two groups, and one-factor *ANOVA* was used for comparison between multiple groups when the obtained data were by a normal distribution; otherwise, Welch *ANOVA* test was used. If results were statistically significant, differences were analyzed by the *LSD* method or *Dunnett's T3* test. It was used to indicate that the difference was statistically significant when a*P*-value of less than 0.05 (*P*<0.05) .

3. Results and discussion

Preparation and characterization of PAA-Fe$_3$O$_4$ and CSO-PAA-Fe$_3$O$_4$

PAA was combined with Fe$_3$O$_4$ nanoparticles, and then CSO was linked through amide bonds to prepare CSO-PAA-Fe$_3$O$_4$ nanoprobes. Learnt from Figure 2a$_1$ and 2b$_1$, PAA-Fe$_3$O$_4$ and CSO-PAA-Fe$_3$O$_4$ were spherically shaped and uniform in size. Both nanoparticles showed good dispersion properties, no adhesion, and exhibited a significant increase in particle size from 5.93nm to 8.15nm after the modification of CSO (Figure 2a$_2$ and 2b$_2$). The zeta potentials were also changed with such modification from -31.7 mV for PAA-Fe$_3$O$_4$ to 25.13 mV forCSO-PAA-Fe$_3$O$_4$ (Figure 2a$_3$ and 2b$_3$). In addition, the average hydrodynamic diameter of PAA-Fe$_3$O$_4$ was increased from 95.64 nm to 248.03 nm for CSO-PAA-Fe$_3$O$_4$ (Figure 2a$_4$ and 2b$_4$). The T$_1$ relaxation times of PAA-Fe$_3$O$_4$ and CSO-PAA-Fe$_3$O$_4$ at different concentrations were statistically significantly different (F=1311.83, *P*<0.05; F=1357.21, *P*<0.05). From the data in Figure 2a$_5$ and 2b$_5$, it is apparent that the T$_1$ relaxation time of PAA-Fe$_3$O$_4$ and CSO-PAA-Fe$_3$O$_4$ decreased significantly with the increase of iron ions concentration. And the r_1 relaxation rates of PAA-Fe$_3$O$_4$ and CSO-PAA-Fe$_3$O$_4$ were calculated to be 5.317 m and 6.147 mM $^{-1}$s^{-1}, respectively. Both of the r_1 relaxation rates are better than that of Gd-DTPA, commonly used in clinic, showing their possibility as MRI contrast agent. As Figure 2 c shows, the FTIR spectra further testified the successful modification of CSO onto PAA-Fe$_3$O$_4$ nanoparticles. As shown in Figure 2c, the stretching vibration of C-N bond and tertiary alcohol C-O bond with the absorption peaks at 1321 cm^{-1} and 1155 cm^{-1} were observed on CSO-PAA-Fe$_3$O$_4$ [26]. A prominent absorption peak at 1073 cm^{-1} coming from the stretching vibration absorption peak of C-O bond in the C-O-C structure on the CSO ring could also be detected, showing the existence of CSO in CSO-PAA-Fe$_3$O$_4$. All of the above changes indicated the successful fabrication of CSO-PAA-Fe$_3$O$_4$ nanoprobes.

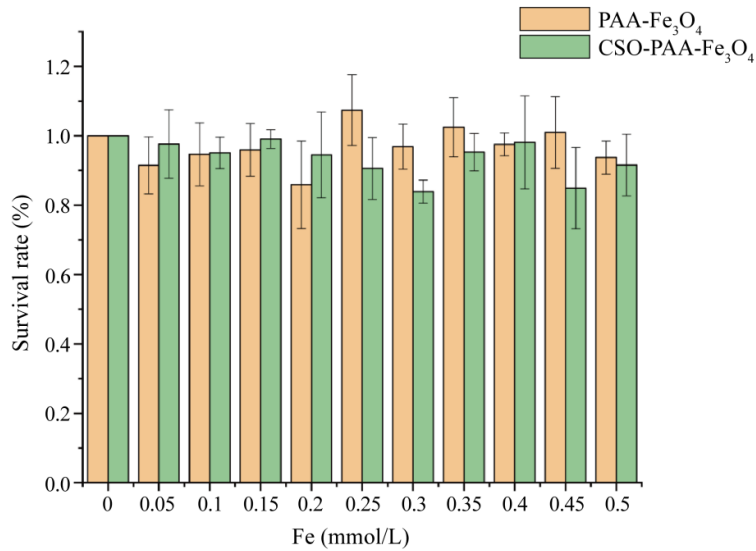### Cytotoxicity assessment of PAA-Fe$_3$O$_4$ and CSO-PAA-Fe$_3$O$_4$

The biocompatibility of PAA-Fe$_3$O$_4$ and CSO-PAA-Fe$_3$O$_4$ were assessed by MTT assay. As showed in Figure 3, there were no significant differences in the absorbance values of RAW264.7 cells neither treated with PAA-Fe$_3$O$_4$ nanoparticles, or with CSO-PAA-Fe$_3$O$_4$ ranging from 0.05~0.50 mmol/L Fe (F=2.138, *P*>0.05; F=1.904, *P*>0.05), indicating no significant cytotoxic influence of PAA-Fe$_3$O$_4$ and CSO-PAA-Fe$_3$O$_4$ on RAW264.7 cell proliferation and desirable biocompatibility.

Oil red O staining to detect the lipidalaggregation in RAW264.7 cells

To show the influence of our fabricated CSO-PAA-
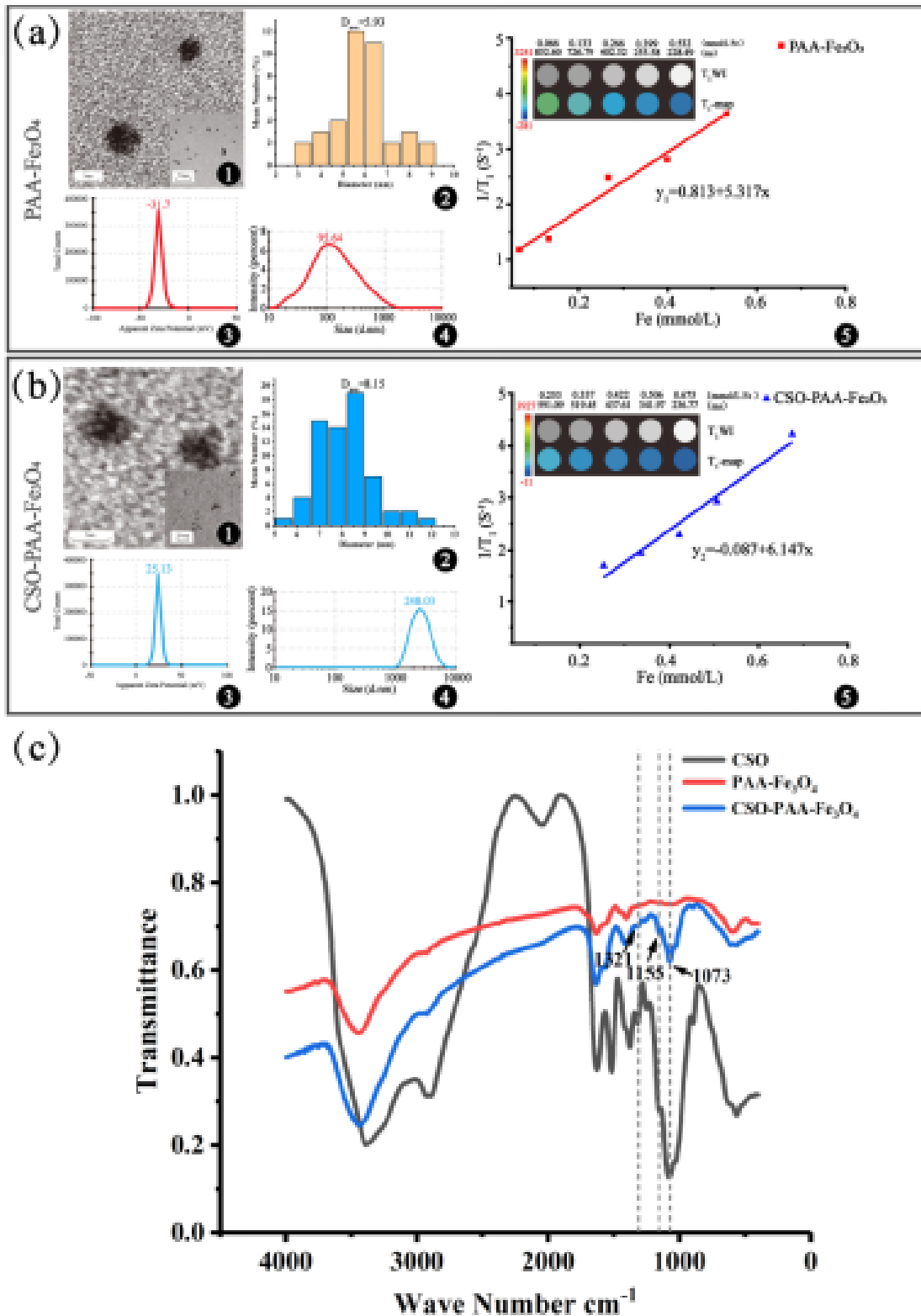
Figure 2. Characterizations of PAA-Fe$_3$O$_4$ (a) and CSO-PAA-Fe$_3$O$_4$ (b). (1-4) TEM observations, particle size distribution, Zeta surface potential distribution, and hydrodynamic diameters of PAA-Fe$_3$O$_4$ and CSO-PAA-Fe$_3$O$_4$. T$_1$-weighted phantom images of PAA-Fe$_3$O$_4$ and CSO-PAA-Fe$_3$O$_4$ at different Fe^{3+} concentrationsand the relaxation rate fit of PAA-Fe$_3$O$_4$ and CSO-PAA-Fe$_3$O$_4$ (5). Fourier transform infrared absorption spectra of PAA-Fe$_3$O$_4$ and CSO-PAA-Fe$_3$O$_4$ (c).

Figure 3. Cytotoxicity assessment of PAA-Fe$_3$O$_4$ and CSO-PAA-Fe$_3$O$_4$ against RAW264.7 ($n=6$).

Fe$_3$O$_4$ nanoprobes on the lipidal accumulation of RAW264.7 cells, 8 groups were set as follows. RAW264.7 cells without any treatment were designated as the blank control group (BLK), and RAW264.7 cells pretreated with 60 μg/mL ox-LDL was set as the model group (NC). RAW264.7 cells pretreated with 60 μg/mL ox-LDL first, and then incubated with different concentrations of PAA-Fe$_3$O$_4$ or CSO-PAA-Fe$_3$O$_4$ were used as experimental groups. As illustrated in Figure 4, compared with the BLK group, the amount of the intracellular lipid accumulation was significantly increased in NC group. And no obvious change of intracellular lipid accumulation between the PAA-Fe$_3$O$_4$ groups and the NC group, showing the little effect of PAA-Fe$_3$O$_4$ on the inhibition of lipid accumulation in RAW264.7 cells. But when compared the PAA-Fe$_3$O$_4$ and CSO-PAA-Fe$_3$O$_4$ groups, the difference was signif-
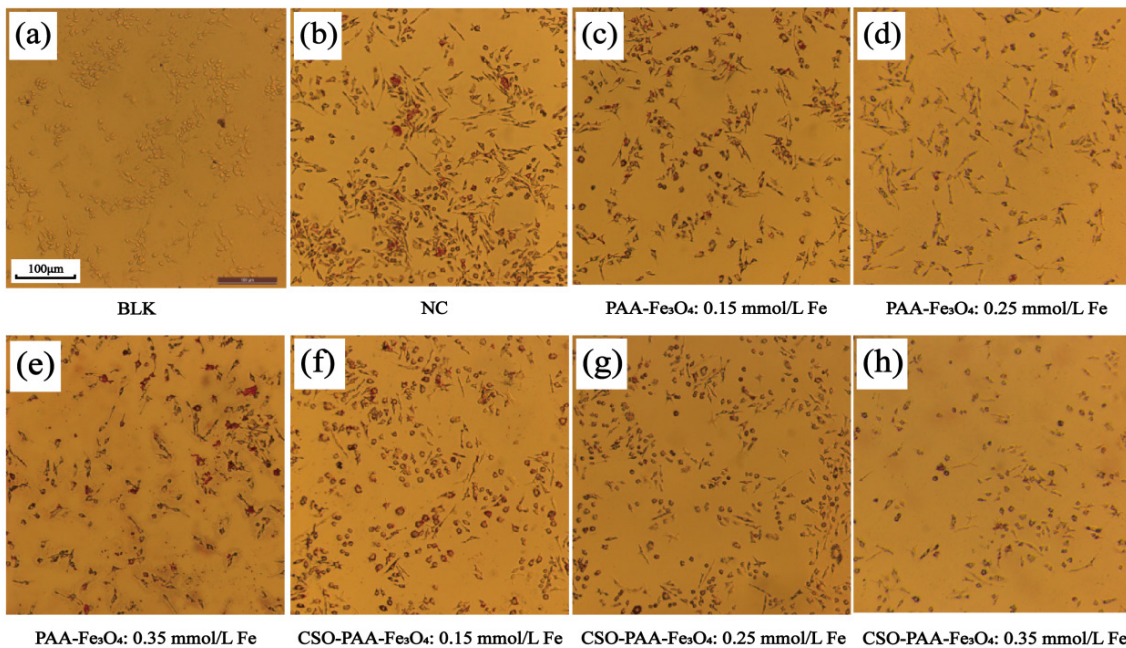
Figure 4. The RAW264.7 cells were stained with oil red O, and the intracellular lipids were stained red. No significant lipid accumulation was observed in the blank control group (a), but significant lipidalaggregation in the model group was shown (b). In PAA-Fe$_3$O$_4$ groups, the lipidalaggregation was unchanged when the iron ion concentration increased (0.15, 0.25 and 0.35mmol/L) (c-e). The lipid accumulation gradually decreased with the increase of iron ion concentration in CSO-PAA-Fe$_3$O$_4$ groups (0.15, 0.25 and 0.35mmol/L) (f-h).

icant and a significant decrease in the intracellular lipid accumulation with a gradual increase of CSO-PAA-Fe$_3$O$_4$. Analysis using ImageJ software further presented such difference semi-quantitatively. The amount of intracellular lipid accumulation in the NC group was significantly higher than that in the BLK group (F=83.108, $P<0.05$). But there was no significant difference in the level of lipid accumulation between the NC group and the PAA-Fe$_3$O$_4$ groups (F=0.694, $P>0.05$) and CSO-PAA-Fe$_3$O$_4$ group with a Fe^{3+} concentration of 0.15 mmol/L (F=12.353, $P>0.05$). However, significant differences existed between the NC group and CSO-PAA-Fe$_3$O$_4$ groups with Fe^{3+} concentratinos of 0.25 and 0.35 mmol/L (F=15.983, $P<0.05$) as well as between CSO-PAA-Fe$_3$O$_4$ groups (F=98.076, $P<0.05$). Such phenomena might come from the existence of CSO and the different amount of CSO in CSO-PAA-Fe$_3$O$_4$ nanoprobes.
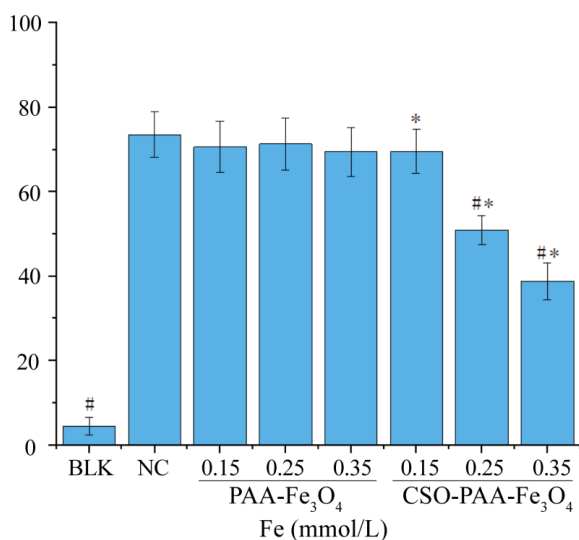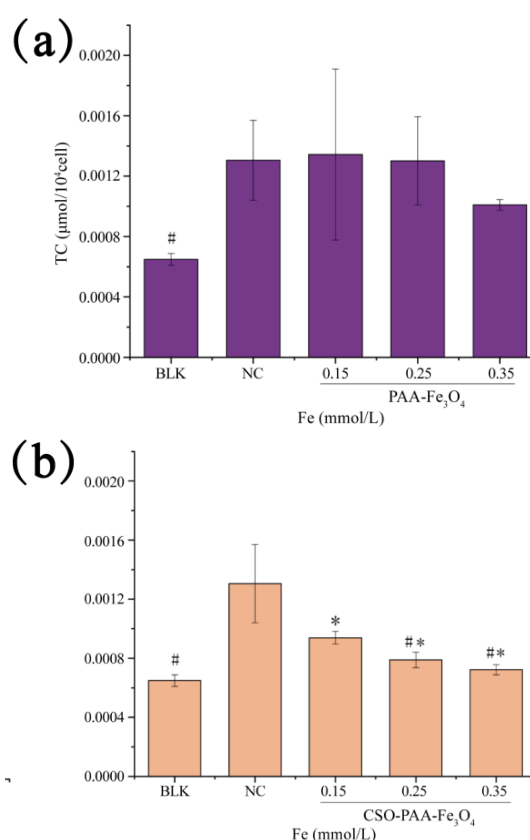

Figure 5. ImageJ analysis of the staining area of RAW264.7 cells by Oil Red O. BLK: Blank group; NC: Model group; #: *P* level less than 0.05 compared with the model group; *: *P* level less than0.05 by paired comparison (*n*=8).

Determination of the TC concentration of RAW264.7 cells

The absorbance values of RAW264.7 cells induced by 60 μg/mL ox-LDL with or without further incubation with PAA-Fe$_3$O$_4$ or CSO-PAA-Fe$_3$O$_4$ at different iron concentrations were determined. It was clearly displayed that compared with the BLK group, there was a remarkable increase in the content of TC in NC group(F=35.910, $P<0.05$). No statistically significant difference of the TC contents in RAW264.7 cells after incubation with PAA-Fe$_3$O$_4$ solutions of different iron concentrations (F=3.306,

$P>0.05$). It presented a significant gradual decreasing trend of TC content in cells after incubated with increasing iron ion concentrations of CSO-PAA-Fe$_3$O$_4$ (F=35.128, $P<0.05$). In Figure 6B, there was noteworthy that CSO-PAA-Fe$_3$O$_4$ with 0.15 mmol/L Fe^{3+} did not produce a significant difference in the TC content between the CSO-PAA-Fe$_3$O$_4$ and NC groups, which is consistent with the results of the previous analysis of the intracellular lipid accumulation content. The difference in the content of TC in the CSO-PAA-Fe$_3$O$_4$ group at different concentrations was statistically significant ($P<0.05$). CSO-PAA-Fe$_3$O$_4$ with 0.25 mmol/L and 0.35 mmol/L Fe^{3+} down-regulated the content of TC in RAW264.7 cells to 62.6% and 56.5%, respectively.

Figure 6. TC concentrations in RAW264.7 cells incubated with different concentration ranges of PAA-Fe$_3$O$_4$ (a) and CSO-PAA-Fe$_3$O$_4$ (b). BLK: blank group; NC: model group; #: *P* level less than 0.05 compared with the model group; *: *P* level less than0.05 by paired comparison (*n*=6).

Specific MRI of RAW264.7 cells in vitro

As Figure 7 showed, there was a significant difference in T$_1$ relaxation time between the blank and experimental groups shown by T$_1$-map color plots. In the Fe^{3+} concentration of 0.25 mmol/L, the T$_1$ relaxation times of PAA-
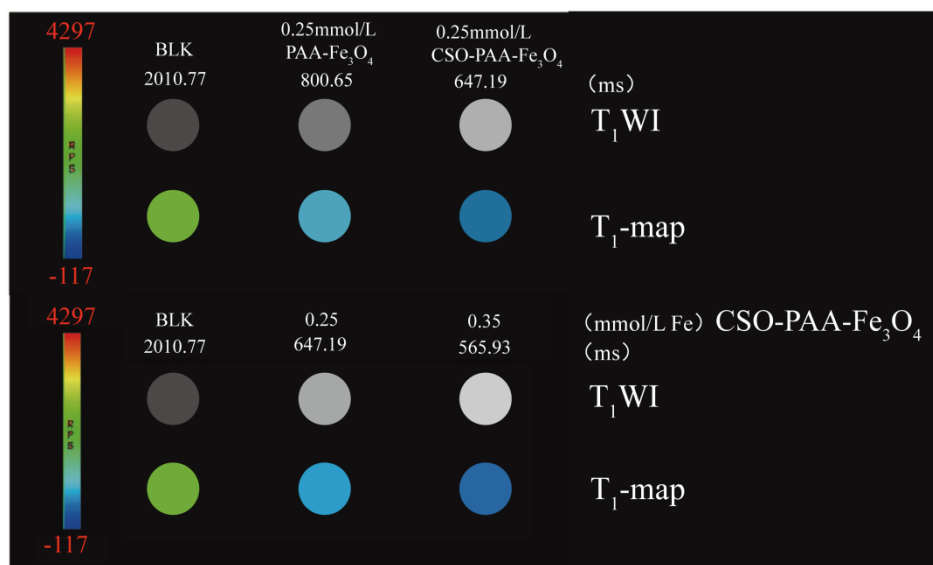
Figure 7. T_1-weighted and T_1-map images of RAW264.7 cells in PBS and different concentration ranges of PAA-Fe$_3$O$_4$ and CSO-PAA-Fe$_3$O$_4$ nanoprobes.

Fe$_3$O$_4$ and CSO-PAA-Fe$_3$O$_4$ group were (800.6 ± 14.30) ms and (647.2 ± 21.91) ms, and the T_1 relaxation time of the PAA-Fe$_3$O$_4$ group was significantly longer than that of the CSO-PAA-Fe$_3$O$_4$ group. One-factor *ANOVA* analysis compared the T_1 relaxation times of the BLK group, 0.25 mmol/L iron ion concentration of PAA-Fe$_3$O$_4$ group, and CSO-PAA-Fe$_3$O$_4$ group, and the differences were statistically significant (F=2418.877, $P<0.05$). Additionally, the T_1 relaxation times of CSO-PAA-Fe$_3$O$_4$ treated cells decreased with the increase of Fe^{3+} concentration (0.15 mmol/L, 0.25 mmol/L, and 0.35 mmol/L), which were (739.4 ± 31.59) ms, (647.2 ± 21.91) ms, and (565.9 ± 26.38) ms, respectively. The results showed that there were statistical differences in T_1 relaxation time between the BLK group and CSO-PAA-Fe$_3$O$_4$ group for each Fe^{3+} concentration (F=2310.838, $P<0.05$). The above MR imaging results showed that the cellular binding amount of CSO-PAA-Fe$_3$O$_4$ was significantly higher than that of PAA-Fe$_3$O$_4$at the same Fe^{3+} concentration, and the cellular binding amount of CSO-PAA-Fe$_3$O$_4$ increased with the increase of nanoprobes. CSO-PAA-Fe$_3$O$_4$ nanoprobes could target RAW264.7 cells and might come from the specific binding of CSO to the mannose receptor of RAW264.7 cells and the endocytosis to achieve the targeted MRI of RAW264.7 cells.

4. Conclusions

In conclusion, targeted MRI and therapeutic nanoprobe based on CSO-PAA-Fe$_3$O$_4$ was successfully designed and was successfully developed. In the process of ox-LDL induction of macrophages, these nanoprobes could effec-tively enter the interior of macrophages and effectively inhibit the transformation of macrophages into foam cells. CSO-PAA-Fe$_3$O$_4$ exhibited good T_1-weighted macrophage targeting MRI capability and a high therapeutic effect on the inhibition of foamy macrophages formation.

Acknowledgements

Conflict of Interest

The paper authors state that there is no conflict of benefits regarding the publication of this article.

References

[1] Adamson PD, Newby DE, Dweck MR(2016)Translational Coronary Atherosclerosis Imaging withPET. CARDIOL CLIN 34 (1):179-186. DOI: 10.1016/j.ccl.2015.06.002.
[2] Huang Y, Coman D, Hyder F, Ali MM(2015)Dendrimer-Based Responsive MRI Contrast Agents (G1-G4) for Biosensor Imaging of Redundant Deviation in Shifts (BIRDS).Bioconjug Chem 26 (12):2315-2323. DOI: 10.1021/acs.bioconjchem.5b00568.
[3] Ibañez B, Badimon JJ, Garcia MJ(2009)Diagnosis of atherosclerosis by imaging.AM J MED 122 (1 Sup-

 DOI: https://doi.org/10.30564/jams.v4i2.3039

pl):S15-S25.

DOI: 10.1016/j.amjmed.2008.10.014.

[4] Cheng D, Wang Y, Liu X, Pretorius PH, Liang M, Rusckowski M, Hnatowich DJ(2010)Comparison of 18F PET and 99mTc SPECT imaging in phantoms and in tumored mice.Bioconjug Chem 21 (8):1565-1570.

DOI: 10.1021/bc1001467.

[5] Hyafil F, Schindler A, Sepp D, Obenhuber T, Bayer-Karpinska A, Boeckh-Behrens T, Höhn S, Hacker M, Nekolla SG, Rominger A, Dichgans M, Schwaiger M, Saam T, Poppert H(2016)High-risk plaque features can be detected in non-stenotic carotid plaques of patients with ischaemic stroke classified as cryptogenic using combined (18)F-FDG PET/MR imaging.Eur J Nucl Med Mol Imaging 43 (2):270-279.

DOI: 10.1007/s00259-015-3201-8.

[6] Vaidyanathan K, Gopalakrishnan S(2017)Nanomedicine in the Diagnosis and Treatment of Atherosclerosis-A Systematic Review.Cardiovasc Hematol Disord Drug Targets 17 (2):119-131.

DOI: 10.2174/1871529X17666170918142653.

[7] Roy TL, Forbes TL, Dueck AD, Wright GA(2018) MRI for peripheral artery disease: Introductory physics for vascular physicians.VASC MED 23 (2):153-162.

DOI: 10.1177/1358863X18759826.

[8] Cromer BS, Kshitiz, Wang CJ, Orukari I, Levchenko A, Bulte JW, Walczak P(2013)Cell motility of neural stem cells is reduced after SPIO-labeling, which is mitigated after exocytosis.MAGN RESON MED 69 (1):255-262.

DOI: 10.1002/mrm.24216.

[9] Richards JM, Shaw CA, Lang NN, Williams MC, Semple SI, MacGillivray TJ, Gray C, Crawford JH, Alam SR, Atkinson AP, Forrest EK, Bienek C, Mills NL, Burdess A, Dhaliwal K, Simpson AJ, Wallace WA, Hill AT, Roddie PH, McKillop G, Connolly TA, Feuerstein GZ, Barclay GR, Turner ML, Newby DE(2012)In vivo mononuclear cell tracking using superparamagnetic particles of iron oxide: feasibility and safety in humans.Circ Cardiovasc Imaging 5 (4):509-517.

DOI: 10.1161/CIRCIMAGING.112.972596.

[10] Ramaswamy S, Schornack PA, Smelko AG, Boronyak SM, Ivanova J, Mayer JJ, Sacks MS(2012) Superparamagnetic iron oxide (SPIO) labeling efficiency and subsequent MRI tracking of native cell populations pertinent to pulmonary heart valve tissue engineering studies.NMR BIOMED 25 (3):410-417.

DOI: 10.1002/nbm.1642.

[11] Gneveckow U, Jordan A, Scholz R, Brüss V, Waldöfner N, Ricke J, Feussner A, Hildebrandt B, Rau B, Wust P(2004)Description and characterization of the novel hyperthermia- and thermoablation-system MFH 300F for clinical magnetic fluid hyperthermia. MED PHYS 31 (6):1444-1451.

DOI: 10.1118/1.1748629.

[12] Zhao Q, Wang L, Cheng R, Mao L, Arnold RD, Howerth EW, Chen ZG, Platt S(2012)Magnetic nanoparticle-based hyperthermia for head & neck cancer in mouse models.THERANOSTICS 2 (1):113-121.

DOI: 10.7150/thno.3854.

[13] Hyung JH, Ahn CB, Il KB, Kim K, Je JY(2016) Involvement of Nrf2-mediated heme oxygenase-1 expression in anti-inflammatory action of chitosan oligosaccharides through MAPK activation in murine macrophages.EUR J PHARMACOL 793:43-48.

DOI: 10.1016/j.ejphar.2016.11.002.

[14] Estelrich J, Sánchez-Martín MJ, Busquets MA(2015) Nanoparticles in magnetic resonance imaging: from simple to dual contrast agents.Int J Nanomedicine 10:1727-1741.

DOI: 10.2147/IJN.S76501.

[15] Khandhar AP, Wilson GJ, Kaul MG, Salamon J, Jung C, Krishnan KM(2018)Evaluating size-dependent relaxivity of PEGylated-USPIOs to develop gadolinium-free T1 contrast agents for vascular imaging.J BIOMED MATER RES A 106 (9):2440-2447.

DOI: 10.1002/jbm.a.36438.

[16] Te BB, van Tilborg GA, Strijkers GJ, Nicolay K(2012)Molecular MRI of Inflammation in Atherosclerosis.Curr Cardiovasc Imaging Rep 5 (1):60-68.

DOI: 10.1007/s12410-011-9114-4.

[17] Peluso G, Petillo O, Ranieri M, Santin M, Ambrosio L, Calabró D, Avallone B, Balsamo G(1994)Chitosan-mediated stimulation of macrophage function. BIOMATERIALS 15 (15):1215-1220.

DOI: 10.1016/0142-9612(94)90272-0.

[18] Hu Z, Shi X, Yu B, Li N, Huang Y, He Y(2018)Structural Insights into the pH-Dependent Conformational Change and Collagen Recognition of the Human Mannose Receptor.STRUCTURE 26 (1):60-71.

DOI: 10.1016/j.str.2017.11.006.

[19] Hou LN, Zhao LH(2006)Binding and stimulatory effect of oligochitosan in macrophages.Journal of China Medical University 35 (2):124-127.

DOI: 10.3969/j.issn.0258-4646.2006.02.006.

[20] Xiang, D(2018)mechanism of chitosan oligosaccalarides inhibiting foam cells formation via autophagy. MA Dissertation, Southwest Medical University.

[21] Jafari H, Bernaerts KV, Dodi G, Shavandi A(2020) Chitooligosaccharides for wound healing biomaterials engineering.Mater Sci Eng C Mater Biol Appl 117:111266.
DOI: 10.1016/j.msec.2020.111266.

[22] Xu Q, Dou J, Wei P(2008)Chitooligosaccharides induce apoptosis of human hepatocellular carcinoma cells via up-regulation of Bax.Carbohydrate Polymers: Scientific and Technological Aspects of Industrially Important Polysaccharides 71 (4):509-514.

[23] Dou J, Du Y, Tan C(2007)Effects of chitooligosaccharides on rabbit neutrophils in vitro.Carbohydrate Polymers: Scientific and Technological Aspects of Industrially Important Polysaccharides 69 (2):209-213.

[24] Liaqat F, Eltem R(2018)Chitooligosaccharides and their biological activities: A comprehensive review. Carbohydr Polym 184:243-259.
DOI: 10.1016/j.carbpol.2017.12.067.

[25] Kucheryavy P, He J, John VT, Maharjan P, Spinu L, Goloverda GZ, Kolesnichenko VL(2013)Superparamagnetic iron oxide nanoparticles with variable size and an iron oxidation state as prospective imaging agents.LANGMUIR 29 (2):710-716.
DOI: 10.1021/la3037007.

[26] Su YJ, Zhao Q, Sun JZ(2012)Synthesis and Characterization of Chitosan Oligosaccharide-graft-Acrylic Acid Biodegradable Crosslinker.Journal of Chemical Engineering of Chinese Universities 26 (2):285-289.
DOI: 10.3969/j.issn.1003-9015.2012.02.017.